Lagrangian studies in convective turbulence

Jörg Schumacher[*]

Institut für Thermo- und Fluiddynamik, Technische Universität Ilmenau, Postfach 100565, D-98684 Ilmenau, Germany

(Received 3 February 2009; published 4 May 2009)

We present high-resolution direct numerical simulations of turbulent three-dimensional Rayleigh-Bénard convection with a focus on the Lagrangian properties of the flow. The volume is a Cartesian slab with an aspect ratio of four bounded by free-slip planes at the top and bottom and with periodic side walls. The turbulence is inhomogeneous with respect to the vertical direction. This manifests in different lateral and vertical two-particle dispersion and in a dependence of the dispersion on the initial tracer position for short and intermediate times. Similar to homogeneous isotropic turbulence, the dispersion properties depend in addition to the initial pair separation and yield a short-range Richardson-like scaling regime of two-particle dispersion for initial separations close to the Kolmogorov dissipation length. The Richardson constant is about half the value of homogeneous isotropic turbulence. The multiparticle statistics is very close to the homogeneous isotropic case. Clusters of four Lagrangian tracers show a clear trend to form flat, almost coplanar, objects in the long-time limit and deviate from the Gaussian prediction. Significant efforts have been taken to resolve the statistics of the acceleration components up to order four correctly. We find that the vertical acceleration is less intermittent than the lateral one. The joint statistics of the vertical acceleration with the local convective and conductive heat flux suggests that rising and falling thermal plumes are not associated with the largest acceleration magnitudes. It turns out also that the Nusselt number which is calculated in the Lagrangian frame converges slowly in time to the standard Eulerian one.

I. INTRODUCTION

Turbulent convection is one of the best studied fundamental flows in fluid-dynamics research [1,2]. One reason is the large range of examples and applications in nature and technology for which a turbulent motion is initiated and sustained by heating a fluid from below and cooling from above. Almost all of these studies have been conducted in the Eulerian frame of reference. They were primarily focused to the mechanisms of local [3–6] and global [7–10] turbulent heat transfer.

The Lagrangian perspective of turbulence, in which the fields are monitored along the trajectories of infinitesimal fluid parcels, has recently produced new insights into the local topology of fluid parcel tracks, the local strength of accelerations, and the statistics of time increments of turbulent fields [11,12]. The progress is caused on the one hand by significant innovations in the experimental techniques, such as three-dimensional particle tracking [13–15] or acoustic methods [16]. On the other hand, direct numerical simulations of turbulence become now feasible that resolve three-dimensional Lagrangian turbulence at moderate and higher Reynolds numbers [17–20]. Both, experiments and simulations, made a deeper understanding of the small-scale intermittency and its connection with large accelerations of fluid parcels possible.

Lagrangian investigations in convective turbulence are however rare. Several reasons can be given for this circumstance. First, on the experimental side it is desirable to monitor the temperature along the particle tracks beside the velocity components and the accelerations. Only recently, Gasteuil *et al.* [21] constructed therefore a smart particle that monitors velocity, temperature, and orientation while moving through the cell. Due to the integrated power supply the particle diameter remained however larger than the thermal boundary layer thickness, such that the large-scale bulk motion can be monitored only. Second, it is also clear that the complexity of direct numerical simulations increases since the temperature field has to be advected in addition to the velocity. Temperature tracking along the tracer positions requires additional interpolations. Furthermore, one cannot return to simulations in a fully periodic cube, the so-called homogeneous Rayleigh-Bénard convection setup, since the periodicity in the direction of the mean temperature gradient causes a self-amplifying fluid motion. This was discussed in detail by Calzavarini *et al.* [22,23]. Third, the turbulence is inhomogeneous—at least in the vertical direction as in the following setup—and it is thus not clear which of findings from the homogeneous isotropic purely hydrodynamic turbulence pertain. For example, the height dependence of the statistics has to be considered additionally.

First numerical attempts have been made recently to study some aspects of the heat transfer and tracer dispersion in the Lagrangian framework of convective turbulence [24]. The motivation of the study can be condensed in one question: Which new insight into the nature of turbulent convection provides the complementary Lagrangian view? One result of [24] was to determine a mixing zone which is dominated by rising and falling thermal plumes. This is done by combining acceleration and local convective heat flux statistics. The mixing zone starts right above the thermal boundary layer and extends several tens of the boundary layer thickness into the bulk of the cell. Thermal plumes are fragments of the thermal boundary layer that detach in the vicinity of the top and bottom isothermal planes. The existence of a mixing zone has been suggested in several Eulerian studies on the

---

*joerg.schumacher@tu-ilmenau.de

basis of other criteria, e.g., [25,26] and was thus confirmed in the complementary Lagrangian frame of Ref. [24].

The present work extends the previous study [24] into several directions. Besides the local convective, the local conductive heat flux is studied along the tracer tracks. It requires to monitor temperature gradient components. Furthermore, the analysis of the Lagrangian tracer dispersion is extended. In addition to the hydrodynamic case [20], we study the dependence of pair dispersion on the initial separation *and* the initial seeding position. As discussed in Refs. [19,27,28] for the pure hydrodynamic case, higher-order particle statistics requires to track little clusters of tracers. We provide here an analysis of the four-particle statistics, where the tracers start out of groups of tetrahedra of different sidelengths and initial vertical positions.

The outline of the manuscript is as follows. In Sec. II the equations of motion, the numerical scheme, the Lagrangian tracer tracking, and the turbulent heat transfer are discussed. In Sec. III, some results of the Eulerian statistics of the temperature field are presented. This section is followed by sections on the Lagrangian particle dispersion, the acceleration statistics, and the conductive and convective heat flux. We conclude with a short discussion of our results and will give a brief outlook to possible extensions of the present work.

II. NUMERICAL MODEL

A. Equations of motion and boundary conditions

The Boussinesq equations, i.e., the Navier-Stokes equations for an incompressible flow with an additional buoyancy term $\alpha g \theta \boldsymbol{e}_z$ and the advection-diffusion equation for the temperature field, are solved by a standard pseudospectral method for the three-dimensional case [29]. The equations are given by

$$\boldsymbol{\nabla} \cdot \boldsymbol{u} = 0, \tag{1}$$

$$\frac{\partial \boldsymbol{u}}{\partial t} + (\boldsymbol{u} \cdot \boldsymbol{\nabla})\boldsymbol{u} = -\boldsymbol{\nabla} p + \nu \boldsymbol{\nabla}^2 \boldsymbol{u} + \alpha g \theta \boldsymbol{e}_z, \tag{2}$$

$$\frac{\partial \theta}{\partial t} + (\boldsymbol{u} \cdot \boldsymbol{\nabla}) \theta = \kappa \boldsymbol{\nabla}^2 \theta + u_z \frac{\Delta T}{H}. \tag{3}$$

Here, $\boldsymbol{u}$ is the turbulent velocity field, p is the (kinematic) pressure field, and θ is the temperature fluctuation field. The system parameters are: gravity acceleration g, kinematic viscosity ν, thermal diffusivity κ, vertical temperature gradient $\Delta T/H$, and thermal-expansion coefficient α. The temperature field is decomposed into a linear profile and fluctuations θ about the profile

$$T(\boldsymbol{x}, t) = -\frac{\Delta T}{H}(z - H/2) + \theta(\boldsymbol{x}, t). \tag{4}$$

Since T is prescribed and constant at bottom and top boundaries $z=0$ and $z=H$, the condition $\theta=0$ follows there. Here, $\Delta T > 0$. The dimensionless control parameters are the Prandtl number Pr, the Rayleigh number Ra, and the aspect ratio Γ,

$$\mathrm{Pr} = \frac{\nu}{\kappa}, \tag{5}$$

$$\mathrm{Ra} = \frac{\alpha g H^3 \Delta T}{\nu \kappa}, \tag{6}$$

$$\Gamma = \frac{L}{H}. \tag{7}$$

The simulation domain is $V = L \times L \times H = [0, \Gamma \pi] \times [0, \Gamma \pi] \times [0, \pi]$. In lateral directions x and y, periodic boundary conditions are taken. In the vertical direction z, free-slip boundary conditions are used which are given by

$$u_z = \theta = 0 \quad \text{and} \quad \partial_z u_x = \partial_z u_y = 0. \tag{8}$$

The computational grid has a size of $N_x \times N_y \times N_z = 2048 \times 2048 \times 513$ points. For an aspect ratio $\Gamma = 4$, it is thus equidistant in all three space directions with a grid spacing Δx. Time stepping is done by a second-order predictor-corrector scheme. The production runs are conducted on one rack of the Blue Gene/P system which corresponds with 4096 MPI tasks [29]. We use volumetric fast Fourier transforms based on the p3dfft package by Pekurovsky [30]. The spectral resolution is $k_{\max}\eta_K = 4.5$, where $k_{\max} = 2\sqrt{2}\pi N_x/(3L_x)$. Quantity $\eta_K = \nu^{3/4}/\langle\epsilon\rangle^{1/4}$ is the Kolmogorov scale with the mean energy dissipation rate $\langle\epsilon\rangle$.

B. Lagrangian particle tracking

Lagrangian tracer particles follow the streamlines of the turbulent velocity field in correspondence with

$$\dot{\boldsymbol{x}} = \boldsymbol{u}(\boldsymbol{x}(t), t). \tag{9}$$

For the majority of the analysis, we seeded 3×10^5 tetrahedra aligned along the outer coordinate axes in the box, i.e., $\boldsymbol{x}_1 = \boldsymbol{x}_0$, $\boldsymbol{x}_2 = \boldsymbol{x}_0 + \ell \boldsymbol{e}_x$, $\boldsymbol{x}_3 = \boldsymbol{x}_0 + \ell \boldsymbol{e}_y$, and $\boldsymbol{x}_4 = \boldsymbol{x}_0 + \ell \boldsymbol{e}_z$. The vector $\boldsymbol{x}_0$ is randomly chosen in the box. The tracer ensemble was divided into six groups with initial sidelengths of $\ell = 1, 2, 4, 8, 16,$ and 32 grid spacings Δx, which correspond with 0.5, 1, 2, 4, 8, and 16 η_K. The two-particle dispersion analysis is consequently conducted for the three tracer pairs $\{\boldsymbol{x}_1, \boldsymbol{x}_2\}$, $\{\boldsymbol{x}_1, \boldsymbol{x}_3\}$, and $\{\boldsymbol{x}_1, \boldsymbol{x}_4\}$ of each tetrahedron.

For the two-particle and multiparticle statistics, we run in addition a simulation with the following initial conditions: again $\boldsymbol{x}_1 = \boldsymbol{x}_0$, $\boldsymbol{x}_2 = \boldsymbol{x}_0 + \ell \boldsymbol{e}_x$, $\boldsymbol{x}_3 = \boldsymbol{x}_0 + \ell \boldsymbol{e}_y$, and $\boldsymbol{x}_4 = \boldsymbol{x}_0 + \ell \boldsymbol{e}_z$. The x and y coordinates of vector $\boldsymbol{x}_0$ are again randomly chosen. The vertical coordinate corresponds with $z_0 = \delta_T/2$, δ_T, $10\delta_T$, $20\delta_T$, and $H/2$. Here, we pick $\ell = \eta_K/2$ and $2\eta_K$.

The Lagrangian particles are advanced in time simultaneously with the Boussinesq equations. The velocity, temperature, and temperature gradient components at intergrid positions are calculated by trilinear interpolation. The full particle set is written out each 0.45 τ_η. Here, $\tau_\eta = \sqrt{\nu/\langle\epsilon\rangle}$ is the Kolmogorov time. Accelerations along the Lagrangian tracks are calculated from three successive integration steps ($\Delta t = 0.006 \tau_\eta$) and the output interval is the same as for the particle positions, velocities, temperature, and temperature gradient. We thus gather Lagrangian statistics over up to 4.8×10^8 tracer particle events. Figure 1 illustrates the initial phase of the tracer dispersion. All tracers start from a x-y plane close to the bottom wall.
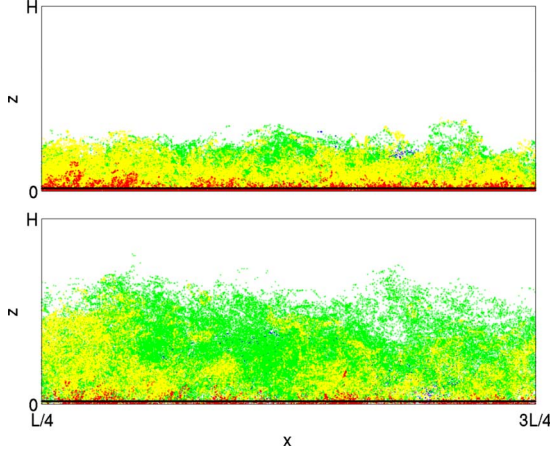
FIG. 1. (Color online) Side view of two instantaneous Lagrangian tracer distributions at $t=9.5\tau_\eta$ (top) and $t=19\tau_\eta$ (bottom). The tracers are colored with respect to the local temperature T at their position. Four intervals are taken: $T \in [\Delta T/2, \Delta T/3]$, $T \in [\Delta T/3, \Delta T/6]$, $T \in [\Delta T/6, 0]$, and $T \in [0, -\Delta T/6]$. The whole ensemble consists of 2×10^5 tracers. Tracers started in the whole x-y plane at the height of the thermal boundary layer thickness which is indicated by the solid line very close to the bottom plane in both plots.

C. Turbulent heat transfer

The convective turbulence is studied for one parameter setting. The Rayleigh number is $Ra = 1.2 \times 10^8$, the Prandtl number $Pr = 0.7$, and the aspect ratio $\Gamma = 4$. The response of the system is a turbulent heat transport as quantified by the dimensionless (Eulerian) Nusselt number which is given for a plane at fixed height z by

$$\mathrm{Nu}(z) = \frac{\langle u_z T \rangle_{A,t} - \kappa \partial_z \langle T \rangle_{A,t}}{\kappa \Delta T / H}, \tag{10}$$

where $\langle \cdot \rangle_{A,t}$ denote averages in planes at z and with respect to time. The value of $\mathrm{Nu}(z)$ is constant and independent of z. The global Nusselt number is then defined as

$$\mathrm{Nu} = \frac{1}{H} \int_0^H \mathrm{Nu}(z) \mathrm{d}z = 1 + \frac{H}{\kappa \Delta T} \langle u_z T \rangle_{V,t}, \tag{11}$$

where $\langle \cdot \rangle_{V,t}$ is a combined volume and time average. The Nusselt number for the present free-slip boundary case follows to $\mathrm{Nu} = 56.36 \pm 0.59$. Similar to Julien *et al.* [31], we find an enhanced turbulent heat transport in comparison to no-slip top and bottom plates. For Rayleigh numbers between 9.8×10^5 and 1.2×10^8, we fit the power law $\mathrm{Nu} = 0.166 \times \mathrm{Ra}^{0.316}$ to the data.

III. EULERIAN TEMPERATURE STATISTICS

Figure 2 displays the mean temperature profile as a function of height. The total temperature can take values between $-\Delta T/2$ and $\Delta T/2$ only. As typical for higher Rayleigh numbers, the jump of mean profile to zero is observed across a thin layer, the thermal boundary layer. The inset magnifies the vicinity of the bottom plate. The thickness of the thermal boundary layer is defined as
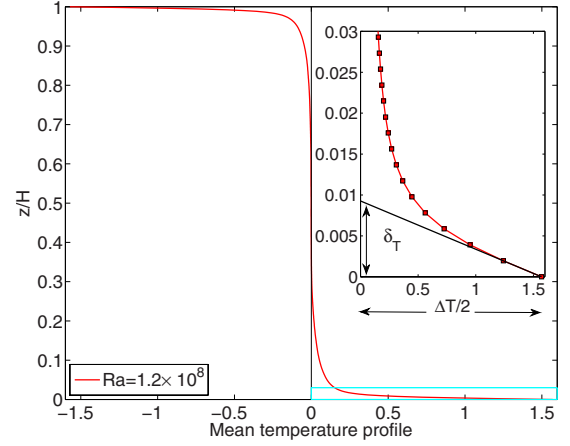

FIG. 2. (Color online) Mean temperature profile $\langle T(z) \rangle_{A,t}$ of the turbulent convection run at $Ra = 1.2 \times 10^8$ and $Pr = 0.7$. The inset shows the resolution of the thermal boundary layer with seven grid planes. It also indicates the geometric interpretation of the thermal boundary layer thickness δ_T (see the text). The lower right box in the main figure indicates the size of the magnification.

$$\delta_T = \frac{H}{2\mathrm{Nu}}. \tag{12}$$

For $z = 0$, the conductive part of Eq. (10) contributes to Nu only and we can set $\mathrm{Nu} = -\kappa \partial_z \langle T \rangle_{A,t}|_{z=0} / (\kappa \Delta T / H)$. This leads to $\delta_T = -\Delta T / (2 \partial_z \langle T \rangle_{A,t}|_{z=0})$ and to the geometric derivation of the thermal boundary layer thickness (as indicated in the inset of Fig. 2). In contrast to the no-slip case, we have $\langle u_x \rangle_{A,t} = \langle u_y \rangle_{A,t} = \langle u_z \rangle_{A,t} = 0$. Consequently, no velocity boundary layer is present. The Taylor microscale Reynolds number $R_\lambda = \sqrt{5/(3\nu\langle\epsilon\rangle)}\langle u_i^2 \rangle \approx 143$.

Figure 3 shows an instantaneous snapshot of the total temperature field $T(\mathbf{x}, t)$. Contour plots in two sideplanes and close to the top and bottom planes are shown. We observe a typical feature of thermal convection—the ridgelike maxima which correspond with thermal plumes that detach randomly. They form a skeleton which is advected by the flow close to the boundaries. The plumes coincide with local maxima of
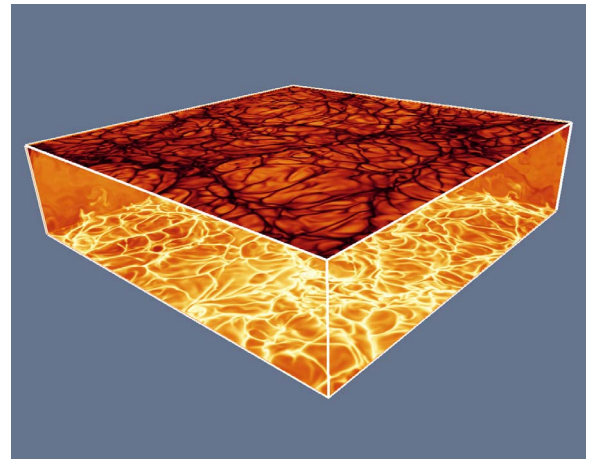

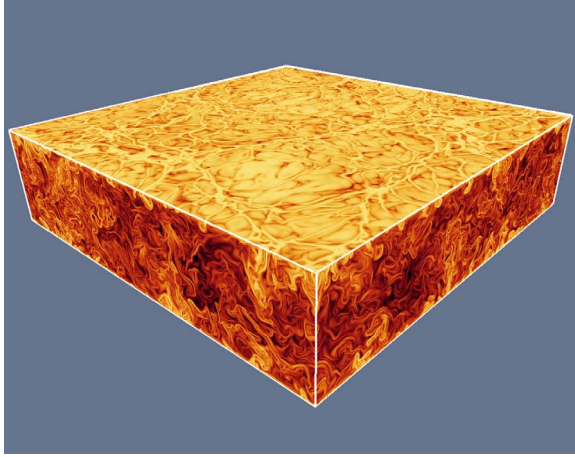FIG. 3. (Color online) Contour plot of the instantaneous temperature field $T(\mathbf{x}, t_0)$.

FIG. 4. (Color online) Contour plot of the instantaneous thermal dissipation rate field $\chi(\boldsymbol{x}, t_0)$. Data correspond to those in Fig. 3. In order to highlight the small-amplitude dissipation filaments in the bulk, we plot contours of the decadic logarithm of χ.

the thermal dissipation rate field (see Fig. 4 and compare it with Fig. 3), which is defined as

$$\chi(\boldsymbol{x}, t) = \kappa [\boldsymbol{\nabla} T'(\boldsymbol{x}, t)]^2. \tag{13}$$

The definition contains the temperature fluctuations which are given by

$$T'(\boldsymbol{x}, t) = T(\boldsymbol{x}, t) - \langle T(z) \rangle_{A,t}. \tag{14}$$

The probability density function (PDF) of T' is shown in Fig. 5. We compare the PDF of data taken from the whole slab volume with the Gaussian statistics in the top figure. Similar to findings for turbulent convection in closed cylindrical vessels with solid walls the temperature field statistics deviates from Gaussian [6]. The analysis can be refined. The inset of the top panel shows therefore vertical profiles of the plane- and time-averaged flatness, $F = \langle T'^4 \rangle_{A,t} / \langle T'^2 \rangle_{A,t}^2$. The flatness differs clearly from the Gaussian value of 3 in all parts of the convection cell. In addition we plot the profile of the plane- and time-averaged skewness $S = \langle T'^3 \rangle_{A,t} / \langle T'^2 \rangle_{A,t}^{3/2}$ in the same inset. The magnitude of the skewness peaks at about $5\delta_T$, which is well inside the plume mixing zone [24]. Both profiles agree also qualitatively with those by Kerr [7] and by Ref. [6], which have been conducted with no-slip top and bottom boundaries. In the bottom panel of Fig. 5 we show the PDF of the temperature fluctuations in four different planes (see the legend). The PDF in the midplane comes closest to a Gaussian profile. Our data suggest that the free-slip boundary conditions lead to smaller deviations from Gaussianity compared to the no-slip case. It should also be noted that for strong rotation of the cell about the vertical coordinate the temperature fluctuations are Gaussian for both no-slip and free-slip boundary conditions, as reported by Julien *et al.* [31].
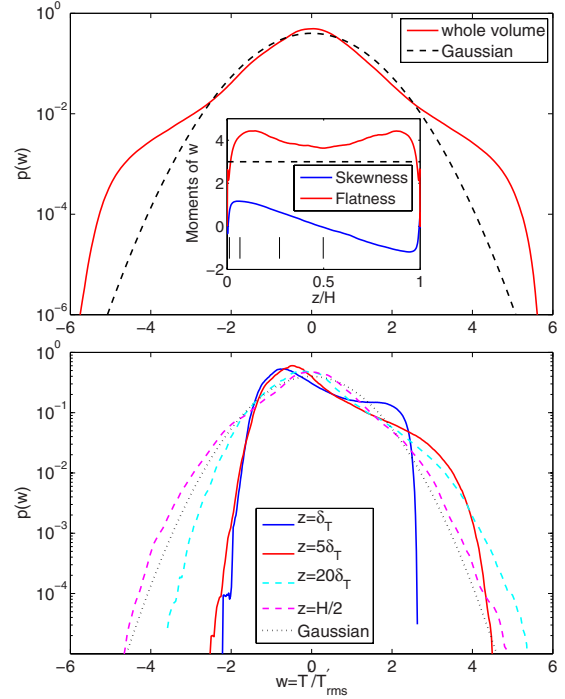

FIG. 5. (Color online) Statistics of the temperature fluctuations $w = T'/T'_{\mathrm{rms}}$. Top: Probability density function (PDF) of the temperature fluctuations. Data are compared with a Gaussian distribution (dashed line). Inset: Skewness and flatness of the temperature fluctuations w as a function of the vertical coordinate z/H. The profiles are obtained by averaging over lateral planes and a sequence of statistically independent snapshots. The Gaussian value for the flatness $F = 3$ is indicated by the dashed line. Bottom: PDFs of the temperature fluctuations taken in different planes which are indicated in the legend and by vertical solid lines in the inset of the top figure.

IV. LAGRANGIAN PARTICLE DISPERSION

A. Two-particle dispersion

The Eulerian framework analysis of turbulent convection demonstrated already that the flow is indeed inhomogeneous with respect to the vertical direction. Furthermore, we recall that the Lagrangian tracer motion is constrained between $z = 0$ and H since both walls cannot be penetrated. One motivation to study the dispersion in three-dimensional turbulent convection is therefore to verify if the classical Richardson dispersion law [32] can be also observed for the present case. Recall that the Richardson dispersion law follows from a solution of a diffusion problem which assumes a homogeneous and isotropic turbulent state. It states that, given two-particle tracks, $\boldsymbol{x}_2(t)$ and $\boldsymbol{x}_1(t)$ with $\boldsymbol{x}_i = (x_i, y_i, z_i)$, the distance vector $\boldsymbol{R}(t) = \boldsymbol{x}_2(t) - \boldsymbol{x}_1(t)$ will follow

$$\langle R^2(t) \rangle_L = g_{3d} \langle \epsilon \rangle t^3, \tag{15}$$

where g_{3d} is a universal constant of $\mathcal{O}(1)$. The symbol $\langle \cdot \rangle_L$ denotes an average over Lagrangian particle tracks. We decompose the relative tracer motion into a lateral and vertical contribution in order to separate homogeneous and inhomogeneous directions. The distance vector can be written as
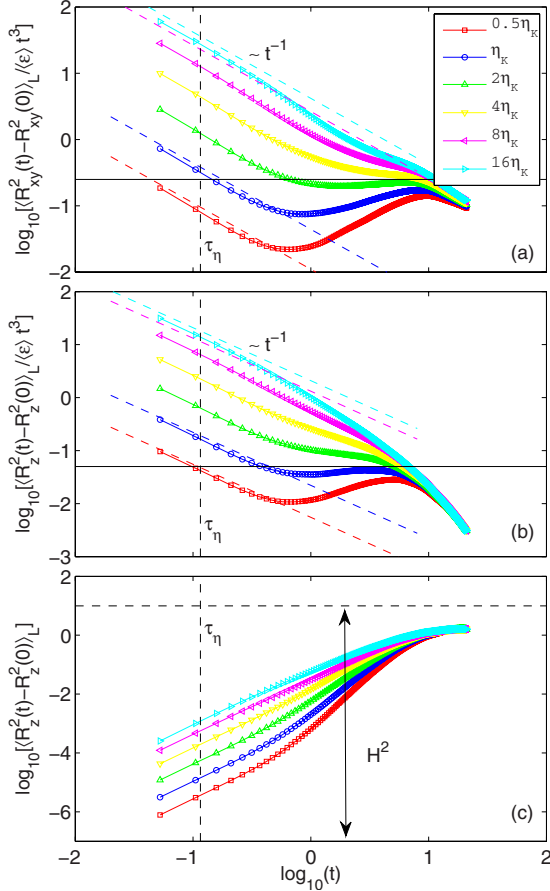
FIG. 6. (Color online) Vertical and lateral particle pair dispersion as a function of the initial pair separation. (a) Compensated lateral dispersion for different initial separations as indicated in the legend. The dashed lines correspond with Eq. (18) for $R_0 = \eta_K/2$ and $R_0 = \eta_K$ and with the Eq. (19) for $R_0 = 8\eta_K$ and $R_0 = 16\eta_K$. (b) Compensated vertical dispersion. Again, Eqs. (18) and (19) are fitted to the data for the same initial separations. (c) Same data as in (b) without compensation by $\langle\epsilon\rangle t^3$. The vertical dispersion is constrained between the planes and levels thus off at larger times. The square of the cell height, H^2, and the Kolmogorov time scale, τ_η, are indicated. All axes are given in decadic logarithm. Tracer pairs are seeded initially across the whole volume.

$$\mathbf{R}(t) = \mathbf{R}_{xy}(t) + R_z(t)\mathbf{e}_z. \tag{16}$$

The lateral two-particle dispersion is given by $\langle R^2_{xy}(t) - R^2_{xy}(0)\rangle_L$, where the average is taken over 6×10^5 particle pairs. Here,

$$\mathbf{R}_{xy} = [x_2(t) - x_1(t)]\mathbf{e}_x + [y_2(t) - y_1(t)]\mathbf{e}_y. \tag{17}$$

Similarly, the vertical dispersion is given by $\langle R^2_z(t) - R^2_z(0)\rangle_L$. The dispersion in each space direction would contribute with a weight of 1/3 in homogeneous isotropic turbulence. In order to compare our pair dispersion results with the predictions for isotropic turbulence, we will introduce two weight factors, $C_{xy} = 2/3$ for the lateral motion and $C_z = 1/3$ for the vertical one.

Figure 6 displays both dispersion processes with respect

to time for six different initial pair separations as explained in Sec. II C. The two-particle dispersion is given by a compensated plot in panels (a) and (b) of the figure. The graphs are normalized by $\langle\epsilon\rangle t^3$ to capture a Richardson-like scaling as a plateau. The initial ballistic behavior at small separations causes then an algebraic decay with t^{-1}. Following Sawford *et al.* [20], we fit the following two relations to our data at small times

$$\frac{\langle R^2_m(t) - R^2_m(0)\rangle_L}{\langle\epsilon\rangle t^3} = \frac{C_m}{3}\left(\frac{R_m(0)}{\eta_K}\right)^2\frac{\tau_\eta}{t} \tag{18}$$

if $R_m(0) \ll \eta_K$ and

$$\frac{\langle R^2_m(t) - R^2_m(0)\rangle_L}{\langle\epsilon\rangle t^3} = \frac{11C_m}{3}C\left(\frac{R_m(0)}{\eta_K}\right)^{2/3}\frac{\tau_\eta}{t} \tag{19}$$

if $\eta_K \ll R_m(0) \ll L$. Here L is the outer scale of turbulence and $C \approx 2$ [20]. Index m stands for the lateral terms, xy, or the vertical term, z. The agreement with Eq. (18) for the initial Kolmogorov and sub-Kolmogorov separations is reasonable. For larger initial separations we use Eq. (19). The larger the initial separation the better the agreement of prediction and data. We fitted the two smallest and largest initial separations only. None of the initial separations is neither much smaller nor much larger than the Kolmogorov scale, which explains the slight deviations of the numerical results from laws (18) and (19).

As discussed for example in Refs. [20,33], the establishment of a Richardson-like regime depends sensitively on the initial separation between the tracers. Indeed, for one of the six different separations the lateral dispersion curve passes through a small plateau with a Richardson constant $g_{xy} \approx 0.25$. This is observed for an initial separation of $R_{xy}(0) = 2\eta_K$ [see solid line in Fig. 6(a)]. The re-translation of the proportionality constant g_{xy} into a three-dimensional homogeneous isotropic turbulence case is obtained by

$$\tilde{g}_{xy} = \frac{g_{xy}}{C_{xy}} = \frac{3}{2}g_{xy} \approx 0.375. \tag{20}$$

The proportionality constant is smaller than the value $g_{3d} \approx 0.5-0.6$ for homogeneous isotropic turbulence [18–20]. In Ref. [24], it was already shown that the PDF of the lateral particle pair distance can be fitted to the stretched exponential form of Richardson [32], however not to the Gaussian shape as suggested by Batchelor [34].

Figures 6(b) and 6(c) display the vertical dispersion. In panel (b), we repeat the compensated plot of panel (a) and show the fits to Eq. (18). A plateau is observed now for initial separations between $1\eta_K$ and $2\eta_K$. The resulting constant is $g_z \approx 0.05$ [see solid line in Fig. 6(b)]. If one combines the lateral and vertical dispersion, the Richardson constant for the turbulent convection follows to

$$g_{xy} + g_z \approx 0.3, \tag{21}$$

which is less than our earlier estimate of $\tilde{g}_{xy} \approx 0.375$ and $g_{3d} \approx 0.5-0.6$. A smaller Richardson constant corresponds with a stronger correlated pair motion. Such behavior can be attributed to the presence of rising and falling thermal plumes—a feature that is absent in isotropic turbulence. Ad-
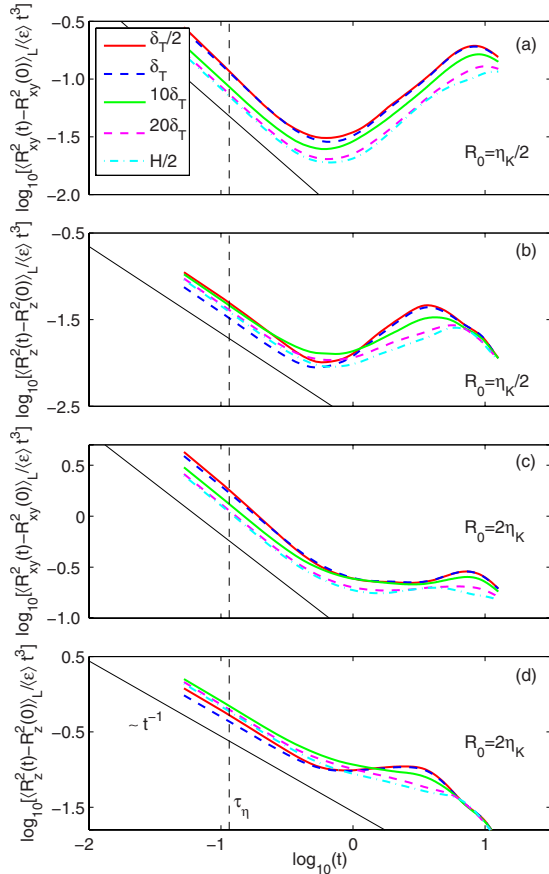
FIG. 7. (Color online) Vertical and lateral particle pair dispersions as functions of the initial vertical seeding position z_0. (a) Compensated lateral dispersion for different initial heights z_0 as indicated in the legend (holds for all four figures). The initial tracer separation is $R_0 = \eta_K/2$. (b) Compensated vertical dispersion. The initial separation is also $R_0 = \eta_K/2$. (c) Compensated lateral dispersion. The initial separation is now $R_0 = 2\eta_K$. (d) Compensated vertical dispersion. Again $R_0 = 2\eta_K$. All axes are given in decadic logarithm and the Kolmogorov time scale is indicated by a dashed line. The solid line follows $\sim t^{-1}$ in all plots.

ditionally, it is known that the plumes can cluster and form a large-scale circulation [2]. Figure 6(c) demonstrates that the vertical dispersion is constrained by the top and bottom planes. The vertical contribution $\langle R_z^2(t) - R_z^2(0) \rangle_L$ to the pair dispersion levels off. Eventually the lateral dispersion contributes solely to the long-time behavior.

The specifics of the present inhomogeneous flow is that not only the initial pair separation, but also the initial seeding position is important. This brings us to the second series of particle dispersion studies where tracer pairs with fixed distance in different horizontal planes of the slab are seeded (see Sec. II C for details) and shorter simulations for about half the duration are rerun. Figure 7 summarizes our findings. We picked five initial seeding heights: two in the boundary layer and two in the plume mixing zone [24] and the center plane. While panels (a) and (b) are for $R_0 = \eta_K/2$, panels (c) and (d) are for $R_0 = 2\eta_K$. The latter is the separation that yielded a short Richardson-like range in Fig. 6(a).

Figures 7(a) and 7(c) show that the lateral dispersion curves of the tracer subgroups differ in magnitude. The local slope is however nearly the same for all subsets. The situation is slightly different for the vertical dispersion: while the seeding in the center plane causes a gradual variation in the local slope of the dispersion curve [see Figs. 7(b) and 7(d)], the seeding in the thermal boundary layer leads to significant differences after the initial ballistic period. The same result is observed in Fig. 7(d). The reason is that the tracer pairs probe then the detachment of the boundary layer fragments to full extent. This is not the case when starting in the bulk of the cell. It can also be observed that a plateau (which would imply Richardson-like scaling) depends sensitively on the initial separation and seeding height.

To summarize this part, Richardson-like dispersion appears for a very small range of scales in the present flow. Similar to previous studies, we confirm that the initial pair dispersion depends sensitively on both the initial pair separation and the initial vertical position of a tracer pair in the volume. The qualitative behavior of the tracer dispersion in the convection flow is very similar to that in homogeneous isotropic turbulence, given the same range of Reynolds numbers. The specifics of the turbulence, such as the particular driving mechanism or a present inhomogeneity, manifests however in the proportionality constant g_{3d} and causes eventually quantitative deviations from homogeneous isotropic turbulence. Figure 7(c) illustrates this fact very nicely. The scatter of the plateaus can be interpreted as a measure of the sensitivity.

B. Multiparticle statistics

The Lagrangian statistics of higher-order moments requires to follow more than two Lagrangian tracers simultaneously. In the following, we will focus to the four-particle case. The tracers are initially seeded at the edges of tetrahedra as discussed in Sec. II C. The distortion of such a small particle cluster by the turbulence has been studied for the pure hydrodynamic case in Refs. [19,27,28,35]. The original motivation for such analysis was to get a deeper geometrical insight into the formation of frontlike structures in scalar turbulence: in the vicinity of steep scalar gradients small particle clusters become co-planar. Furthermore, since the cluster evolution probes the whole range of scales of turbulence, one hopes to disentangle systematically correlated large-scale advection from decorrelated small-scale motion. The presence of thermal plumes in convection will alter the deformation of the cluster at small times. It is however open, what will be observed in the long-time limit.

The particle tracks $\boldsymbol{x}_1(t)$, $\boldsymbol{x}_2(t)$, $\boldsymbol{x}_3(t)$, and $\boldsymbol{x}_4(t)$ can be transformed into the center-of-mass coordinate

$$\boldsymbol{r}(t) = \frac{1}{4}\sum_{i=1}^{4}\boldsymbol{x}_i(t), \qquad (22)$$

and the three relative coordinates (which are of interest here)

$$\boldsymbol{\rho}_1(t) = \frac{1}{\sqrt{2}}[\boldsymbol{x}_2(t) - \boldsymbol{x}_1(t)],$$

$$\boldsymbol{\rho}_2(t) = \frac{1}{\sqrt{6}}[2\boldsymbol{x}_3(t) - \boldsymbol{x}_1(t) - \boldsymbol{x}_2(t)],$$
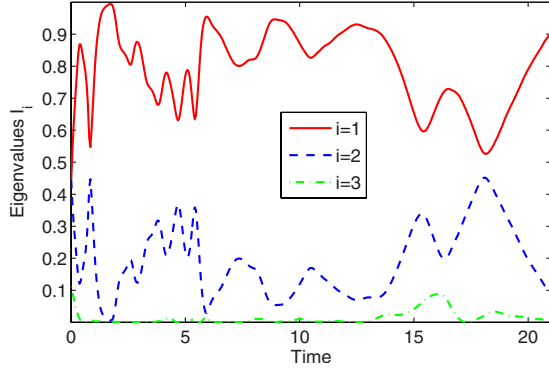
FIG. 8. (Color online) Time evolution of the eigenvalues I_i [see Eq. (25) for their definition] of one particular four-particle cluster.

$$\boldsymbol{\rho}_3(t) = \frac{1}{\sqrt{12}}[3\boldsymbol{x}_4(t) - \boldsymbol{x}_1(t) - \boldsymbol{x}_2(t) - \boldsymbol{x}_3(t)]. \qquad (23)$$

The radius of gyration follows in this frame to $R_g = \sqrt{\rho_1^2 + \rho_2^2 + \rho_3^2}$. The shape evolution of the particle cluster is monitored by the following moment-of-inertia tensor:

$$g^{ab} = \sum_{i=1}^{3} \rho_i^a \rho_i^b, \qquad (24)$$

where $a, b = x, y, z$ is the component index of the vector $\boldsymbol{\rho}_i$ and $i = 1, 2, 3$. The real eigenvalues $g_1 \geq g_2 \geq g_3 \geq 0$ quantify the shape of the particle cluster. Isotropic objects correspond with $g_1 = g_2 = g_3$, cigar-shaped clusters with $g_1 \gg g_2 \approx g_3$ and pancake-shaped clusters with $g_1 \approx g_2 \gg g_3$. Figure 8 shows the time evolution of the three eigenvalues for one specific four-particle cloud. The eigenvalues are normalized and given by

$$I_k = \frac{g_k}{\sum_{m=1}^{3} g_m} \quad \text{for} \quad k = 1, 2, 3. \qquad (25)$$

Thus $0 \leq I_k \leq 1$. One can observe that the eigenvalue variations become smoother with increasing time. A convergence of the cluster to an almost coplanar object is observable for larger times, as quantified by the small value of I_3. It will turn out now that this example displays a typical long-time behavior.

In Fig. 9, we show the time evolution of the Lagrangian ensemble average of the normalized eigenvalues. Data for different initial sidelengths of the tetrahedra are compared. The tetrahedra are seeded across the whole volume. Similar to the two-point measure, the initial deformation of the clusters depends sensitively on the sidelength of the tetrahedron. The smaller the initial sidelength the stronger the initial stretching of the cluster to a cigar-shaped object (for $t \lesssim 15\tau_\eta$). After about $87\tau_\eta$ all curves collapse and the mean values remain almost unchanged. Our data yield $\langle I_1 \rangle_L = 0.84$, $\langle I_2 \rangle_L = 0.15$, and $\langle I_3 \rangle_L = 0.01$. Surprisingly, the obtained mean values are very close to the findings of Biferale *et al.* [19] and Hackl *et al.* [36] for homogeneous isotropic turbulence. In Ref. [19], tetrahedra were excluded that had two points too close or too far of each other such that their values are
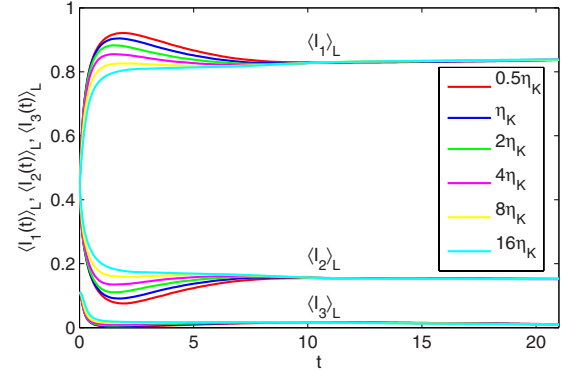

FIG. 9. (Color online) Time evolution of the normalized eigenvalues of the moment-of-inertia tensor. The average is taken over the whole ensemble of tetrahedra. For times $t > 10 (= 87\tau_\eta)$ the data converge to values $\langle I_3 \rangle_L \to 0.84$, $\langle I_2 \rangle_L \to 0.15$, and $\langle I_1 \rangle_L \to 0.01$. The tetrahedra are seeded in the whole volume initially.

not directly comparable with the present ones. Recent three-dimensional particle tracking experiments by Lüthi *et al.* [37] report an $\langle I_2 \rangle_L$ which is also close to 0.16.

Since the large scales are probed in the long term limit by the particle clusters, this agreement suggests that convective and isotropic turbulences on this scale do not differ significantly. The relative motion within a cluster is insensitive to whether the tracer particles are swept by large vortex structures or by large-scale circulation. Consequently, our findings suggest that the constrained vertical motion (and thus the inhomogeneity) is not important in the diffusive long-time limit of the cluster dynamics.

One can expect that for times $t > 10^2 \tau_\eta$, the tracers advance independently of each other. The present long-time means are compared with the result of a joint Gaussian distribution of the relative coordinates, $p(\boldsymbol{\rho}_1, \boldsymbol{\rho}_2, \boldsymbol{\rho}_3) \sim \exp[-(\rho_1^2 + \rho_2^2 + \rho_3^2)]$. This ansatz results to $\langle I_1 \rangle_G = 0.75$, $\langle I_2 \rangle_G = 0.22$, and $\langle I_3 \rangle_G = 0.03$ for the three-dimensional case which is obtained by Monte Carlo simulations [28]. The reported mean of $\langle I_2 \rangle_L = 0.15$ is smaller than the Gaussian value.

Figure 10 reports the dependence of the shape evolution from the initial position z_0. The effects remain small, but systematic. The closer the starting position of the tetrahedron to the boundary plane, the faster it converges into the final quasistatic state. Again the stretching and deformation is most efficient when the particle cluster passes through the mixing zone right above the thermal boundary layer.

Figure 11 displays the PDFs of I_k for five instants $t > 87\tau_\eta$. The plots highlight two aspects. First, there is still a big variety in the amplitudes of individual I_k although their means remain almost unchanged. Second, a very slow drift in the tails is present which is indicated by the arrows in Figs. 8(a) and 8(c).

V. ACCELERATION STATISTICS

The top panel of Fig. 12 shows the PDFs of the three acceleration components. Each component is given in units of the corresponding root-mean-square value. As expected,
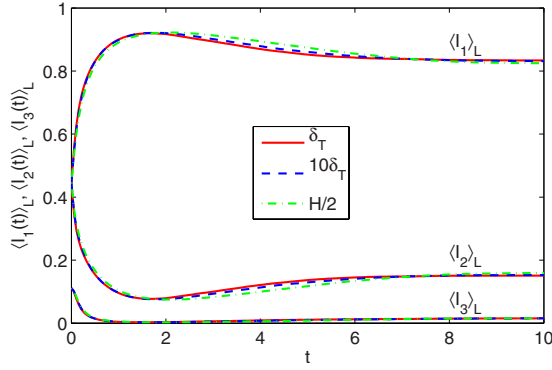
FIG. 10. (Color online) Time evolution of the normalized eigen-values of the moment-of-inertia tensor. The average is taken again over the whole ensemble of 5×10^4 tetrahedra for each case. Four tracer particles form initially a tetrahedron with a sidelength of $\eta_K / 2$. Three ensembles started in planes with δ, $10\delta_T$, and $H/2$ as given in the legend.

the distributions of the two lateral components coincide. Table I provides the quantitative details of the acceleration statistics and lists for example the skewness $S(a_k) = \langle a_k^3 \rangle / \langle a_k^2 \rangle^{3/2}$ and the flatness $F(a_k) = \langle a_k^4 \rangle / \langle a_k^2 \rangle^2$ with $k = x, y$ or z. The numbers for the lateral components are almost
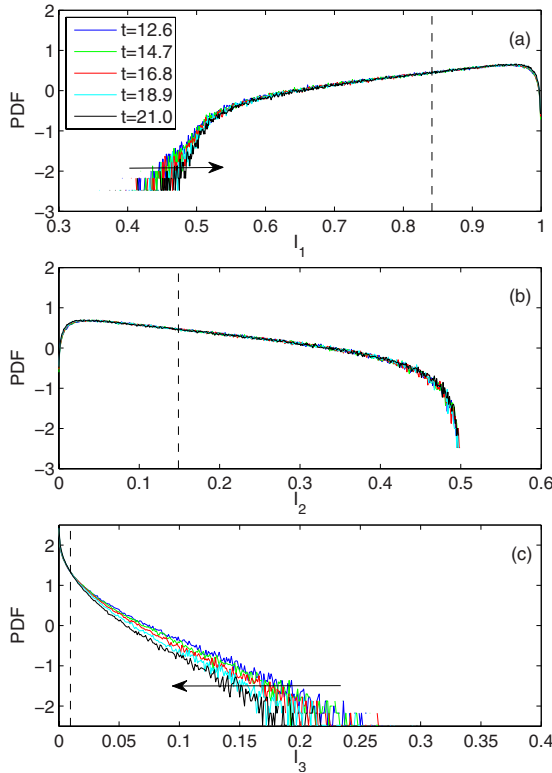
FIG. 11. (Color online) Probability density functions of the nor-malized eigenvalues I_k of the moment-of-inertia tensor (a) I_1, (b) I_2, and (c) I_3. The time instants at which the data have been analyzed are for $t > 87\tau_\eta$ as given in the legend in (a). The vertical dashed lines mark the long-time averages $\langle I_k \rangle_L$. The arrows in the upper and lower panel indicate that there is still a slight drift in the tails al-though the means in Fig. 9 remain nearly unchanged. The tetrahedra are seeded again in the whole volume initially.
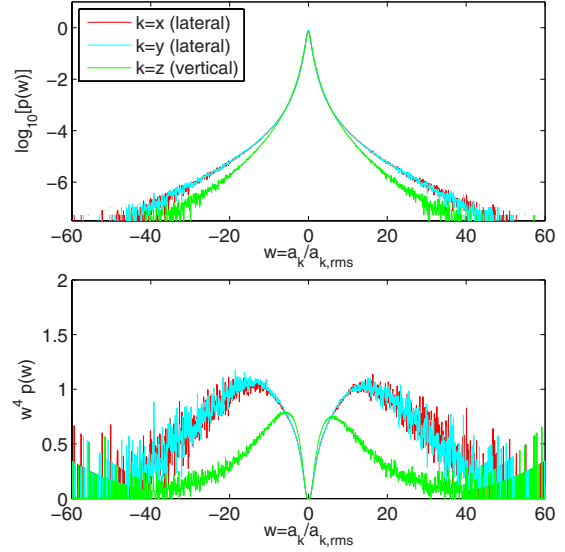

FIG. 12. (Color online) Probability density function (PDF) of acceleration components a_k with $k = x, y$ and z. Upper panel: PDF plots. Each component is normalized by its corresponding root-mean-square value. Lower panel: Statistical convergence test for the fourth moment of the acceleration. The total number of events which as been included for the analysis are 4.4×10^8.

identical. The vertical acceleration component has a smaller flatness which is in line with a sparser tail of the correspond-ing PDF. The bottom panel of the same figure provides the statistical convergence test of the fourth-order moments where the product $w^4 p(w)$ is plotted vs w with $w = a_k / a_{k,\mathrm{rms}}$. It reflects the fundamental difficulty to gather reliable statis-tics for higher-order moments in Lagrangian turbulence. Re-call that this analysis is conducted over a set of 4.4×10^8 events. The area which is occupied by the scatter of the graphs in the tails of the PDFs determines the error bar of the fourth-order moment (and consequently of the flatness). We checked that the second and third-order moments display almost no scatter (not shown). The issue of statistical con-vergence has been discussed for turbulence measurements in a swirling flow [38,39] and in numerical simulations of ho-mogeneous isotropic turbulence [40]. Our values for the flat-ness $F(a_k)$ of the lateral flatness are of the same magnitude as those reported in [38].

Figure 13 refines the statistical analysis of the acceleration components. Due to the vertical inhomogeneity, we report

TABLE I. Root-mean-square values, total maximum/minimum amplitudes, skewness $S(a_k) = \langle a_k^3 \rangle / \langle a_k^2 \rangle^{3/2}$, and flatness $F(a_k) = \langle a_k^4 \rangle / \langle a_k^2 \rangle^2$ of the acceleration components. The error bars of $F(a_k)$ have been obtained by measuring the area of the scatter in the lower panel of Fig. 12. Maxima and minima are given in units of the gravity acceleration g.

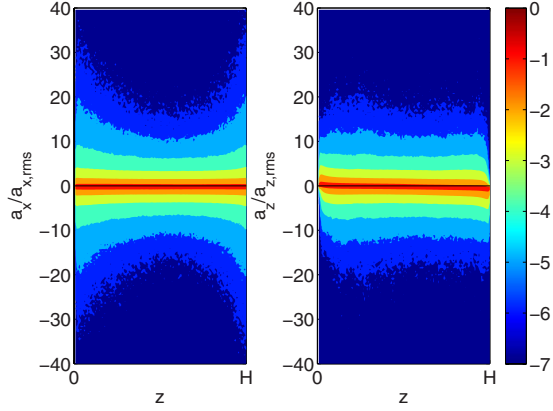|	$\sqrt{\langle a_k^2 \rangle}$	$\frac{\max(a_k)}{g}$	$\frac{\min(a_k)}{g}$	$S(a_k)$	$F(a_k)$
a_x	1.17	1001	−574	−0.093	63.4(±16)
a_y	1.16	559	−540	−0.156	64.4(±16)
a_z	1.10	518	−680	−0.119	30.3(±11)

FIG. 13. (Color online) Joint probability density function of acceleration components a_i and the height z. Left: component a_x. Right: component a_z. The contours are displayed units of the decadic logarithm. The normalization of the acceleration component in both panels is as in Fig. 12.
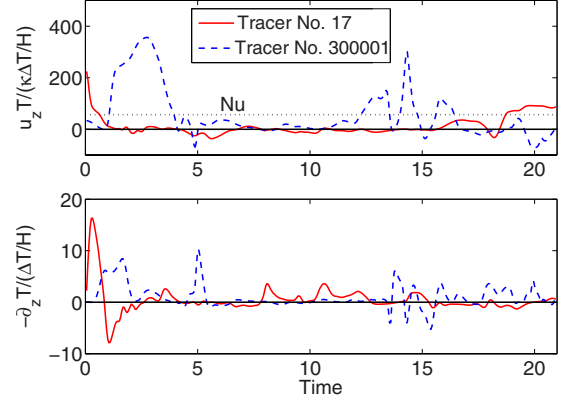

FIG. 14. (Color online) Time traces of the convective (top) and conductive (bottom) heat transfer along two of the 1.2×10^6 tracers. The Eulerian value of Nu is indicated as a dotted line in the top panel.

the height dependence of the acceleration statistics for one lateral and the vertical component, respectively, and plot contours of the joint PDF $p(a_i, z)$. The largest lateral accelerations and the fattest tails are found close to the top and bottom planes. It will turn out in Sec. VI that the vorticity is concentrated in cyclones and anticyclones close to the thermal boundary layer which can rationalize the large lateral accelerations. The support of the PDF decreases monotonically to the center plane. We will get back to this point later in the text when discussing the role of the vertical vorticity component in connection with plume detachments. In contrast to the result for the lateral accelerations, the support of the joint PDF $p(a_z, z)$ shows no significant variation with height. It shrinks to zero in the boundary planes (since is $u_z \equiv 0$) and grows rapidly up to about the thermal boundary layer thickness. The slight asymmetry of the inner contour lines (for the largest probability density levels) corresponds with the rising plumes which detach from the bottom plane at $z = 0$ and have $a_z > 0$ and with falling plumes at $z = H$ for which $a_z < 0$. Note also that the support of all PDFs is the same in the center of the cell. This is consistent with the idea that the turbulence is close to isotropic far away from the isothermal walls.

The important result of this section is that there is differently strong intermittency for the vertical and lateral accelerations in thermal convection. It is caused by the higher level of intermittency in and close to the thermal boundary layer. As a consequence, we will have to take a closer look at the mechanisms of local heat transfer in the vicinity of the top and bottom planes. This is done in Sec. VI.

VI. LAGRANGIAN CONVECTIVE AND CONDUCTIVE HEAT FLUX

A. Lagrangian heat flux

The local heat flux contributions can be probed in the Lagrangian frame of reference. We adopt therefore definition (10) and calculate the local Lagrangian conductive and convective flux contributions. They are given by

$$\mathrm{Nu}(\boldsymbol{x}) = \mathrm{Nu}_{\mathrm{conv}}(\boldsymbol{x}) + \mathrm{Nu}_{\mathrm{cond}}(\boldsymbol{x}) = \frac{H}{\kappa \Delta T}[u_z(\boldsymbol{x})T(\boldsymbol{x}) - \kappa \partial_z T(\boldsymbol{x})],$$
(26)

along the Lagrangian tracks $\boldsymbol{x}(t)$. Figure 14 shows typical time traces of $\mathrm{Nu}_{\mathrm{conv}}$ and $\mathrm{Nu}_{\mathrm{cond}}$ along two tracers. They display a big variability with respect to time. Even negative values are possible for both contributions. As expected, the convective term has a significantly larger magnitude than the conductive one. The latter is dominant in the thermal boundary layers where the thermal dissipation rate χ has the largest magnitude. Figure 15 displays the PDFs of the convective and conductive contributions gathered along the tracks of the whole tracer ensemble. In addition, we display the results for the products $u_x T$ and $u_y T$. All quantities are shown in units of their root-mean-square values. While the PDFs for $u_x T$ and $u_y T$ are symmetric, those of $u_z T$ and $\kappa \partial_z T$ are strongly skewed. This reflects the vertical net transfer of heat through the volume. The Lagrangian average $\mathrm{Nu}_L = \langle \mathrm{Nu}(\boldsymbol{x}) \rangle_{L,t}$ results to

$$\mathrm{Nu}_L = 1 + \frac{H}{\kappa \Delta T} \langle u_z T \rangle_{L,t}.$$
(27)

We have directly verified from the corresponding PDF in Fig. 15(c) that the mean of the Lagrangian conductive heat transfer is with 1.04 very close to one. Furthermore, it is found that $\mathrm{Nu}_L < \mathrm{Nu}$. This is in contrast to the experimental findings for the smart particle probe of Gasteuil *et al.* [21], where $\mathrm{Nu} < \mathrm{Nu}_L$. The reason for this difference might be due to the finite extension of the smart particle that exceeded the thickness of the thermal boundary layer. We have compared the result for the full record (F) with that of a smaller subset (S), which is one third of set (F) and the results differed by 6.5% only (see also Fig. 15). A time-resolved analysis shows that $\mathrm{Nu}_L(t) = \langle \mathrm{Nu}(\boldsymbol{x}, t) \rangle_L$ relaxes slowly to the Eulerian value of Nu. The tracers which have been seeded randomly or at particular heights at the beginning have to pass a kind of "thermalization" process.
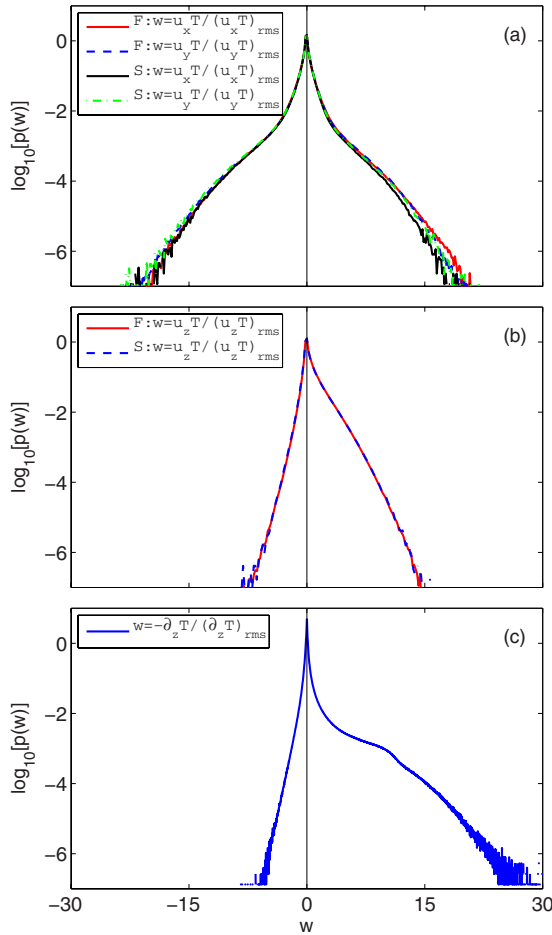
FIG. 15. (Color online) Probability density functions (PDF) of the conductive and conductive heat flux contributions along the Lagrangian tracer tracks. (a) Lateral convective contributions $u_x T$ and $u_y T$. (b) Vertical convective contribution $u_z T$. (c) Conductive contribution $-\partial T / \partial z$. All quantities are normalized by their root-mean-square values. The analysis is conducted over two different data sets: the full record (F) and a third of it (S).

Our result sheds interesting light on the joint velocity-temperature sampling properties of the Lagrangian tracers. First, it is known that for the present geometry a large-scale circulations are present [41,42]. Tracers will preferentially follow the circulation motion in the convection layer. The large-scale circulation can carry a fraction of the total heat transport only, as has been analyzed recently with a proper orthogonal decomposition [43]. Second, we observe high-amplitude events of the vertical vorticity $\omega_z = \partial_x u_y - \partial_y u_x$ close to the maxima of the thermal dissipation rate χ. This is shown in Figs. 16 and 17 where contour plots of slice snapshots of χ and ω_z at a height $z = \delta_T$ are compared. The local maxima in dissipation rate plot (16) reproduce the skeleton of plume sheets. In their vicinity, we observe cyclones and anticyclones that are generated in connection with the detachment of plume fragments. This observation is in line with results in [5] for the nonrotating and with [31] for the rotating case. Exactly these cyclones and anticyclones cause the large lateral positive and negative accelerations as seen in the PDFs in Fig. 12. Figure 18 plots vertical profiles of means of both quantities. While the root-mean square of the
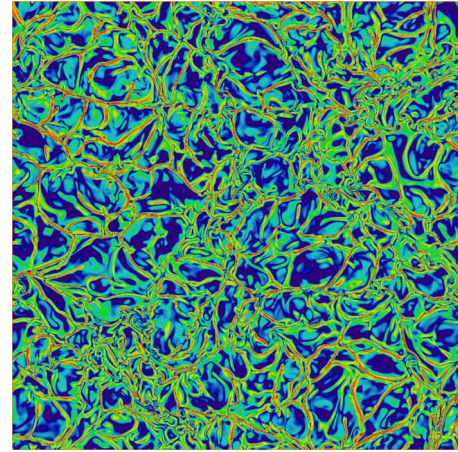

FIG. 16. (Color online) Contour plot of the decadic logarithm of the thermal dissipation rate $\log_{10}[\chi(x,y,z=\delta_T,t_0)]$. The logarithmic contour spacing is chosen in order to highlight the small-amplitude events.

vertical vorticity component varies weakly, the thermal dissipation rate is strongly peaked in and close to the boundary layer. It is also known from studies in homogeneous isotropic turbulence [11] that the Lagrangian tracers are not very frequently trapped in the core of such vortex structures.

B. Joint statistics of Lagrangian heat flux and acceleration

The thermal plumes detach permanently from the thermal boundary layer and can be identified as regions in which the product $u_z T' > 0$ [21,24]. Here we extend this analysis and study the correlations between the vertical velocity component and the (total) temperature in relation to the acceleration. Figure 19 displays the joint statistics of the vertical and lateral accelerations and the products of velocity and temperature, $u_z T$. In order to highlight the statistical correlation between the two variables of the joint PDF we divide the joint PDF by the two single quantity PDFs,
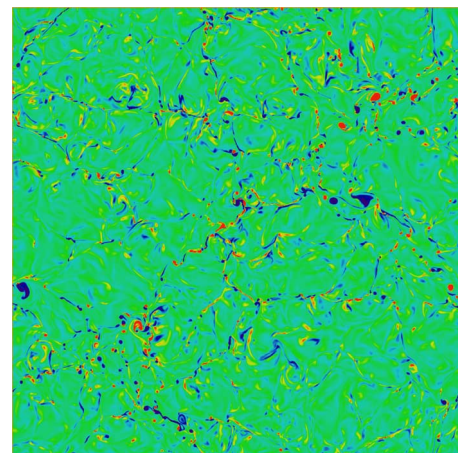

FIG. 17. (Color online) Contour plot of the vertical vorticity component $\omega_z(x,y,z=\delta_T,t_0)$. Data correspond to those in Fig. 13.
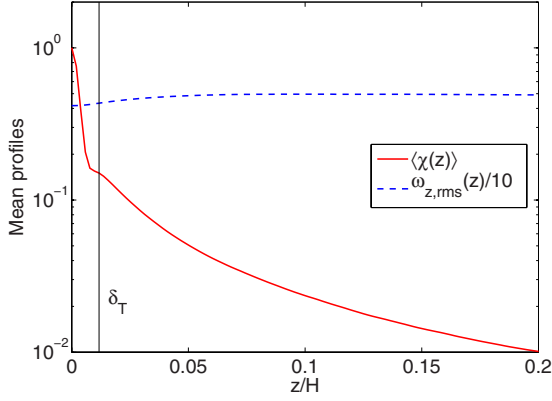
FIG. 18. (Color online) Vertical profiles of the averaged thermal dissipation rate $\langle \chi(z) \rangle_{A,t}$ (solid line) and the root-mean square of vertical vorticity component $\sqrt{\langle \omega^2(z) \rangle_{A,t}}$ (dashed line). The latter is divided by a factor of 10.

$$\Pi(a_i, u_z T) = \frac{p(a_i, u_z T)}{p(a_i)p(u_z T)}. \tag{28}$$

The top panel of Fig. 19 shows the joint statistics for a_x and $u_z T$. A pronounced maximum at larger accelerations and values of $u_z T$ is found. They can be related to coherent structures, such as vorticity tubes in the bulk of the slab or the cyclones/anticyclones in the boundary layer. The correlation between vertical acceleration and the product $u_z T$ is weaker. The local amplitudes of the joint PDF are found at the outer boundaries of the support, at moderate acceleration amplitudes and larger values of $u_z T$. In Ref. [24], we reported the same behavior for $p(a_z, u_z T')$ and identified rising plumes ($a_z > 0$, $u_z T' > 0$) and falling plumes ($a_z < 0$, $u_z T' > 0$). Recirculations around rising and falling plumes have to form due to the incompressibility of the fluid. They were related to
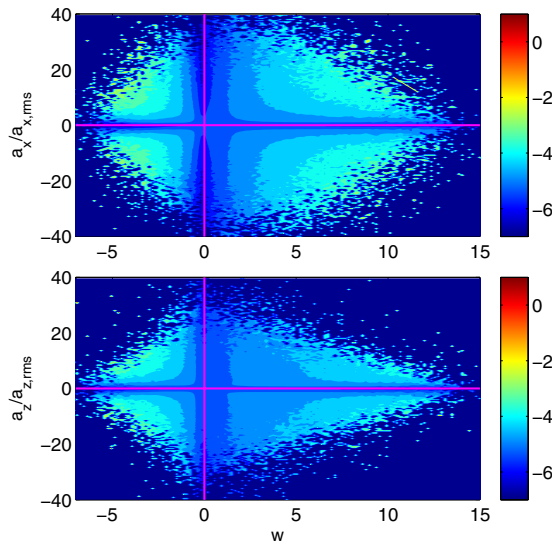

FIG. 19. (Color online) Joint probability density function of lateral acceleration (upper panel) and vertical acceleration (lower panel) and heat flux contributions. Upper panel: $w = u_z T/(u_z T)_{\rm rms}$. Lower panel: $w = u_z T/(u_z T)_{\rm rms}$. The contour spacing is in decadic logarithm.
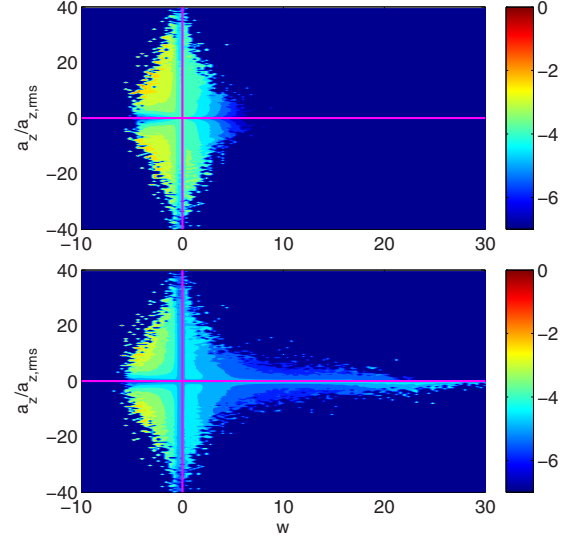

FIG. 20. (Color online) Joint probability density function of the vertical acceleration component $a_z/a_{z,\rm rms}$ and $w = -\partial_z T/(\partial_z T)_{\rm rms}$. Top panel: Tracer positions in the bulk have been considered only. Bottom panel: Tracer positions in the whole volume are included. The contour spacing is in decadic logarithm.

maxima in the half plane $u_z T' < 0$. These are only some of the possible scenarios which can be assigned to strong correlations in the joint statistics. The firm conclusion which we can draw from the present analysis and the one in [24] is that plumes (and therefore the vertical convective flux events) are *not* connected with the largest vertical accelerations. The detachment of plumes is a more gradual process.

We repeated the joint statistical analysis for the conductive part, $-\kappa \partial_z T(\mathbf{x})$. Results are summarized in Fig. 20. The contour plots display now

$$\Pi(a_z, -\partial_z T) = \frac{p(a_z, -\partial_z T)}{p(a_z)p(-\partial_z T)}. \tag{29}$$

We keep in mind from Eqs. (10) and (26) that upward conductive heat transport events have a negative sign, i.e., $-|\partial_z T|$. While the lower panel of Fig. 20 includes the Lagrangian data of the whole volume, the upper panel of the same figure excludes events in the thermal boundary layer up to the beginning of the plume mixing zones. This zone was identified and studied in [24] and starts for the present parameter setting at a height $H/16$. The extended tail in the lower panel can thus be related to largest gradients (and thus largest thermal dissipation rate amplitudes) in and above the thermal boundary layer. The asymmetry to negative a_z for the largest gradients can be interpreted as tracer decelerations which are present when temperature gradients are formed. Negative accelerations (or decelerations) seem to be frequently related to stagnation-point flow topologies, those flows which can make the temperature field steep to large gradients.

VII. SUMMARY AND DISCUSSION

The focus of the present work was on Lagrangian aspects of turbulent convection. The results can be summarized as

follows. The study of pair and multiparticle dispersion yields qualitatively similar results compared to the homogeneous isotropic case. Although the scaling behavior of second-order moments is sensitive to initial separations and seeding heights, initial separations close to the Kolmogorov length result in a short Richardson-like scaling range. Interestingly, we reproduce the same long-time limits for the particle cluster shapes as in isotropic turbulence despite turbulent convection is inhomogeneous. This limit deviates from the Gaussian value. Our results suggest that the dispersion laws can be obtained for more complex flows than isotropic homogeneous turbulence. The proportionality constants are however different, which can be attributed to qualitatively different turbulence structures such as thermal plumes in convection. They affect the vertical dispersion more significantly than the lateral dispersion.

The inhomogeneity of the convective turbulence manifests in less intermittent statistics of the vertical acceleration component compared to the lateral ones. Thermal plumes are not coupled with the strongest accelerations.

We find that the Lagrangian Nusselt number converges slowly to the Eulerian value. A closer inspection of this point could be done in several steps: first, to disentangle the large-scale circulation from the turbulent background, as done in [43], and to combine such a study with a Lagrangian analysis. Second, the present study indicates also that the Nusselt number relaxes faster with a growing number of tracers, in other words the sampling of joint velocity-temperature statistics improves. Our observation is also related to recent experimental and numerical studies at very large Rayleigh numbers [9,44] in which the existence and growth of a so-called superconducting core is discussed, which is in line with a decreasing importance of the large flow circulation for growing Rayleigh numbers. A decreasing importance of a coherent large-scale circulation might lead again to a faster convergence $Nu_L \rightarrow Nu$. More studies of the Lagrangian frame of high-Rayleigh number turbulence are thus necessary.

[1] L. P. Kadanoff, Phys. Today **54**, 34 (2001).

[2] G. Ahlers, S. Grossmann, and D. Lohse, Rev. Mod. Phys. (to be published).

[3] O. Shishkina and C. Wagner, Phys. Fluids **19**, 085107 (2007).

[4] Q. Zhou, C. Sun, and K. Q. Xia, Phys. Rev. Lett. **98**, 074501 (2007).

[5] O. Shishkina and C. Wagner, J. Fluid Mech. **599**, 383 (2008).

[6] M. S. Emran and J. Schumacher, J. Fluid Mech. **611**, 13 (2008).

[7] R. M. Kerr, J. Fluid Mech. **310**, 139 (1996).

[8] J. J. Niemela, L. Skrbek, K. R. Sreenivasan, and R. J. Donelly, Nature (London) **404**, 837 (2000).

[9] G. Amati, K. Koal, F. Massaioli, K. R. Sreenivasan, and R. Verzicco, Phys. Fluids **17**, 121701 (2005).

[10] D. Funfschilling, E. Brown, A. Nikolaenko, and G. Ahlers, J. Fluid Mech. **536**, 145 (2005).

[11] F. Toschi and E. Bodenschatz, Annu. Rev. Fluid Mech. **41**, 375 (2009).

[12] K. R. Sreenivasan and J. Schumacher, Philos. Trans. R. Soc. London (to be published).

[13] S. Ott and J. Mann, J. Fluid Mech. **422**, 207 (2000).

[14] A. La Porta, G. A. Voth, A. M. Crawford, J. Alexander, and E. Bodenschatz, Nature (London) **409**, 1017 (2001).

[15] M. Guala, B. Lüthi, A. Liberzon, A. Tsinober, and W. Kinzelbach, J. Fluid Mech. **533**, 339 (2005).

[16] N. Mordant, P. Metz, O. Michel, and J. F. Pinton, Phys. Rev. Lett. **87**, 214501 (2001).

[17] P. K. Yeung, Annu. Rev. Fluid Mech. **34**, 115 (2002).

[18] G. Boffetta and I. M. Sokolov, Phys. Rev. Lett. **88**, 094501 (2002).

[19] L. Biferale, G. Boffetta, A. Celani, B. J. Devinish, A. Lanotte, and F. Toschi, Phys. Fluids **17**, 115101 (2005).

[20] B. L. Sawford, P. K. Yeung, and J. F. Hackl, Phys. Fluids **20**, 065111 (2008).

[21] Y. Gasteuil, W. L. Shew, M. Gibert, F. Chillá, B. Castaing, and J.-F. Pinton, Phys. Rev. Lett. **99**, 234302 (2007).

[22] E. Calzavarini, D. Lohse, F. Toschi, and R. Tripiccione, Phys. Fluids **17**, 055107 (2005).

[23] E. Calzavarini, C. R. Doering, J. D. Gibbon, D. Lohse, A. Tanabe, and F. Toschi, Phys. Rev. E **73**, 035301(R) (2006).

[24] J. Schumacher, Phys. Rev. Lett. **100**, 134502 (2008).

[25] B. Castaing, G. Gunarante, F. Heslot, L. P. Kadanoff, A. Libchaber, S. Thomae, X.-Z. Wu, S. Zaleski, and G. Zanetti, J. Fluid Mech. **204**, 1 (1989).

[26] S.-Q. Zhou and K.-Q. Xia, Phys. Rev. Lett. **89**, 184502 (2002).

[27] M. Chertkov, A. Pumir, and B. I. Shraiman, Phys. Fluids **11**, 2394 (1999).

[28] A. Pumir, B. I. Shraiman, and M. Chertkov, Phys. Rev. Lett. **85**, 5324 (2000).

[29] J. Schumacher and M. Pütz, in *Proceedings of the International Conference ParCo 2007*, edited by C. Bischof, M. Bücker, P. Gibbon, G. Joubert, T. Lippert, B. Mohr, and F. Peters (IOS Press, Amsterdam, 2007), p. 585.

[30] http://www.sdsc.edu/us/resources/p3dfft/index.php.

[31] K. Julien, S. Legg, J. Mc Williams, and J. Werne, J. Fluid Mech. **322**, 243 (1996).

[32] L. F. Richardson, Proc. R. Soc. London, Ser. A **110**, 709 (1926).

[33] M. Bourgoin, N. T. Ouelette, H. Xu, J. Berg, and E. Bodenschatz, Science **311**, 835 (2006).

[34] G. K. Batchelor, Q. J. R. Meteorol. Soc. **76**, 133 (1950).

[35] J. R. Cressman, W. I. Goldburg, and J. Schumacher, Europhys. Lett. **66**, 219 (2004).

[36] J. F. Hackl, P. K. Yeung, B. L. Sawford, and M. S. Borgas, Bull. Am. Phys. Soc. **53**, 298 (2008).

[37] B. Lüthi, S. Ott, J. Berg, and J. Mann, J. Turbul. **8**, N45 (2007).

[38] G. A. Voth, A. La Porta, A. M. Crawford, J. Alexander, and E. Bodenschatz, J. Fluid Mech. **469**, 121 (2002).

[39] N. Mordant, A. M. Crawford, and E. Bodenschatz, Physica D **193**, 245 (2004).

[40] F. Toschi, L. Biferale, G. Boffetta, A. Celani, B. J. Devenish, and A. Lanotte, J. Turbul. **6**, 40 (2005).

[41] T. Hartlep, A. Tilgner, and F. H. Busse, J. Fluid Mech. **544**, 309 (2005).

[42] M. van Reeuwijk, H. J. J. Jonker, and K. Hanjalić, Phys. Rev. E **77**, 036311 (2008).

[43] J. Bailon-Cuba, M. S. Emran, and J. Schumacher, J. Fluid Mech. (unpublished).

[44] J. J. Niemela and K. R. Sreenivasan, Phys. Rev. Lett. **100**, 184502 (2008).